Soft Matter

PAPER

View Article Online
View Journal

Cite this: DOI: 10.1039/d5sm00933b

Deep learning-driven ultra-stretchable kirigami metamaterials: towards surface texture modulation *via* buckling

Yunce Zhang,[ac] Li Lin,[ac] Yafei Wang,*[b] Shurui Wang,[a] Qiang Tao,[d] Hongwei Liu,[b] Qi Zhang[b] and Changguo Wang*[b]

Kirigami demonstrates distinctive buckling instability behavior when subjected to tensile stress, bestowing the structure with exceptional stretchability and design versatility. Nonetheless, conventional design methodologies predominantly focus on unidirectional cutting kirigami structures, investigating their buckling instability and out-of-plane configurations derived from geometric symmetry. To enhance the functionality of kirigami and thoroughly explore the mechanisms of buckling behavior upon the disruption of geometric symmetry, as well as to comprehend the impact of geometry on programmability during reconfiguration, we have analyzed the buckling instability mechanisms of tessellated cutting kirigami structures. An innovative design strategy for kirigami is proposed, leveraging deep learning techniques to enable accurate predictions of complex nonlinear constitutive relationships. Our approach offers a programmable design framework, facilitating the targeted identification of optimal kirigami structural patterns based on tensile strain requirements, thereby enhancing the adaptability of the desired mechanical response and minimizing trial-and-error costs. Our results indicate a 94.29% accuracy in mechanical performance predictions using the proposed method. The geometric symmetry-breaking considerably broadens the design space for kirigami. Additionally, through cross-selection and functional design of predicted kirigami cells, information encoding and transmission *via* kirigami metasurfaces can be achieved. This paper presents a forward-looking kirigami design strategy that predicts required mechanical performance based on functional demands and enables functional configuration.

Received 15th September 2025,
Accepted 10th November 2025

DOI: 10.1039/d5sm00933b

rsc.li/soft-matter-journal

1 Introduction

The art of kirigami has been extensively integrated into modern scientific and engineering applications, resulting in groundbreaking advancements in flexible electronics[1] and reconfigurable functional surfaces.[2] The fundamental topological design of kirigami significantly drives its applications across diverse fields. Variations in cutting geometric patterns lead to markedly distinct heterogeneous responses in kirigami structures. Furthermore, the mechanical responses of these structures exhibit a strong geometric dependence,[3,4] with minimal influence from other factors such as material properties and scale. This enables kirigami to adhere to its distinctive mechanical mechanisms across various scales and has been utilized in large deployable space structures,[5] architectural facades,[6] stretchable flexible electronics,[7–12] and nanomaterials.[13–15] The interaction among slits is a primary factor contributing to the geometric dependence of kirigami structures on their tensile mechanical properties.[16] Alterations in slit orientation make the coupling between slits increasingly complex and intricate. Although unidirectional cutting kirigami structures exhibit significant stretchability, they often fail to meet the functional demands of flexible electronic devices. Consequently, accounting for variations in slit angles and systematically designing kirigami structures to achieve functionality remains a pressing challenge. By incorporating slit angles into the unidirectional cutting kirigami structure and executing secondary modifications of its geometric patterns, a novel tessellated cutting kirigami structure can be established. This structure, guided by various mechanical deformation mechanisms, can realize various three-dimensional configurations. The intricate geometric formations produced in this manner

[a] School of Architectural Engineering, Harbin University of Science and Technology, Harbin, 150080, P. R. China
[b] Center for Composite Materials and Structures, Harbin Institute of Technology, Harbin 150001, P. R. China. E-mail: wangcg@hit.edu.cn, woofigo@foxmail.com
[c] School of Material Science and Chemical Engineering, Harbin University of Science and Technology, Harbin 150080, P. R. China
[d] College of Mechanical and Electrical Engineering, Qingdao University, Qingdao 266071, P. R. China

can suppress the stretching tendencies of the original unidirectional cutting kirigami structure, thus satisfying both functional requirements and unique mechanical characteristics.

In general, kirigami structures subjected to tensile loading demonstrate in-plane deformation and out-of-plane buckling, progressing through three distinct mechanical response phases: the linear phase, the transitional phase and the hardening phase.[3] The introduction of symmetry-breaking and uneven cutting patterns mitigates adverse boundary effects.[17] Similarly, the pattern in tessellated cutting kirigami structures induces buckling during the stretching phase, revealing a comparable three-stage nonlinear response.[18] Currently, there is a plethora of functional applications inspired by kirigami structures, including self-powered strain sensors,[19] soft crawlers,[20] three-dimensional deformable stents,[21] anti-slip surfaces for footwear,[22] and adaptive imaging.[23] These functionalities are achieved through the buckling and deformation of the sheet and hinges in a low-energy state, facilitating three-dimensional reconfigurability. Despite the importance of geometrically asymmetric cutting patterns in design, the relationship between these patterns and their corresponding mechanical responses remains inadequately explored, indicating a critical need for further investigation to elucidate this essential connection.

Significant advancements have been achieved in theoretical simulation models for geometrically asymmetric unidirectional cutting and geometrically symmetric tessellated cutting kirigami structures.[3,16,24] However, in the case of geometrically asymmetric tessellated cutting kirigami structures, the intricate instability mechanisms can lead to unpredictable mechanical responses and generate a vast design space. Currently, there is an absence of a comprehensive systematic framework to accurately characterize and encompass this design space. Machine learning techniques, characterized by their statistical mechanisms, have emerged as effective tools for analyzing and understanding complex relationships across various domains, including materials science and structural design.[25] This approach effectively dispenses with the traditional "trial-and-error" methodology,[26] facilitating the integration and alignment of geometric parameters with mechanical properties.[27]

Machine learning has demonstrated tremendous potential across various aspects of kirigami. In additive manufacturing, machine learning is employed for defect detection, performance prediction, and adaptive control.[28,29] In the design of metamaterials and metastructures, it can accelerate the discovery and design of novel structures with adaptive capabilities through design optimization and performance prediction.[30–34] Furthermore, machine learning algorithms have been utilized in data-driven simulations to enhance the mechanical properties of structures and achieve functional inverse design by designing microstructures.[35–40] In kirigami design, this technology holds promise for integration with physical knowledge to deepen our understanding of the complex relationship between geometric parameter design and its mechanical response. Through extensive data, machine learning algorithms can accurately identify the delicate connections between the geometric cutting patterns in kirigami structures and their buckling mechanical behavior. In terms of current research, while machine learning has been employed in multiscale kirigami applications, it focuses mainly on the analysis of kirigami structures in terms of tensile deformation.[36,41] There has been a lack of exploration of the instability mechanisms and functional implementations associated with tessellated cutting kirigami structures.

The incorporation of symmetry-breaking enables a programmable deep learning approach that effectively identifies instability modes in kirigami structures.[3] As shown in Fig. 1(a), kirigami exhibits out-of-plane buckling behavior under tensile loading. Through experimental and simulation analysis, the tensile mechanism of tessellated cutting kirigami structures has been elucidated. For instance, as shown in Fig. 1(b), information encryption can be achieved through this mechanism. The letter H is visible in view a, but no useful information is discernible in view b. This enables effective display or hiding of information. A key issue is how to introduce mechanisms to reversely regulate mechanical responses for information encryption.

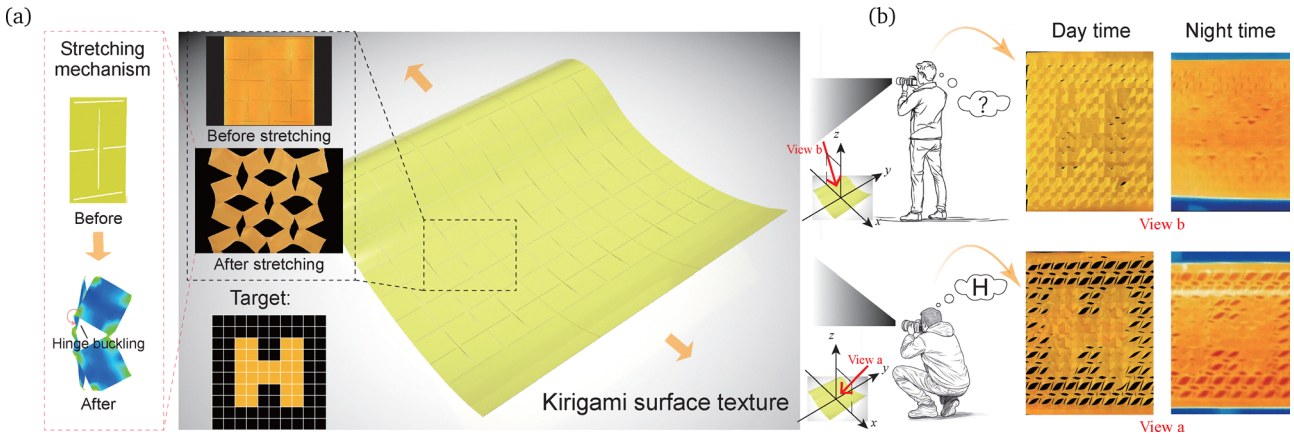

Fig. 1 Schematics of the initial and deformed configurations of kirigami structures. (a) The geometrically symmetric kirigami and its stretching mechanism. (b) Functional design of kirigami surface texture which can be applied to novel information encoding and transmission.

In order to have a higher degree of freedom in direction and dimension, this paper presents a systematic analysis of the buckling mechanical behavior of geometrically asymmetric tessellated cutting kirigami structures. Firstly, the local buckling analysis of the corresponding structure is carried out, and the numerical simulation results are verified by experiments. Then based on the mechanical study of geometrically symmetric kirigami structures, the tensile buckling of geometrically asymmetric kirigami structures is analyzed, and the deep learning-based design method of tessellated cutting kirigami is proposed to obtain the ideal geometric pattern and the corresponding mechanical response. The proposed deep learning method is next introduced to realize the accurate prediction of complex nonlinear constitutive relations. In addition, the mechanical programmability design of the kirigami structure is analyzed. Finally, the functional design of kirigami surface texture is realized by this design method, which can be applied to novel information encoding and transmission.

2 Experimental verification of symmetric kirigami

As shown in Fig. 2, based on the conventional unidirectional cutting kirigami, a tessellated cutting kirigami structure is generated by performing a 90° cutting operation in the gap between the kirigami cutting slits.[3] The unidirectional cutting kirigami structure undergoes tensile buckling with symmetric and antisymmetric localized out-of-plane buckling modes due to the existence of the cutting slits. With the introduction of the cutting slits in the other direction, the overall structure can be divided into two parts: the sheet and the hinge. The plane between the intersecting slits is the sheet, which is connected to form a tessellated cutting kirigami structure through the portion formed by the intersecting slits, *i.e.*, the hinge. As a result, the local buckling modes of the kirigami structure evolve accordingly.[18] In this section, geometrically symmetric kirigami structures are analyzed for tensile buckling.

This section introduces another dimension based on the in-plane deformation of kirigami and investigates how the mechanical buckling behavior of the overall structural system evolves when the thickness phase is very small. When the thickness of kirigami is small, the mechanical instability triggered by uniaxial tensile force can be utilized to create complex 3D patterns and generate persistent creases. From the experiments, it can be found that the buckling modes generated by this instability are significantly influenced by the geometric pattern, which provides a favorable foundation for the realization of functional kirigami designs with a variety of structural properties.

Two typical kirigami structures were tested and numerically simulated to investigate their structural system response under uniaxial tension. The test specimens were made by laser cutting 2×4 mutually perpendicular cutting arrays. Polyimide membrane was used as the material for the test specimens. The membrane contains no hyperelastic constitutive relation. Although the material has plasticity, it is sensitive to cracks. So as a kirigami material, it involves only the elastic stage. This is suitable to exclude the effect of the material on the mechanical properties and thus focus on the geometry–property correlations of the structural system. The uniaxial tensile tests followed the ASTM D882-02 standard and were characterized using an electronic universal materials testing machine (INSTRON-5965). Kirigami strips with a width of 40 mm and a length of 120 mm were fully clamped at both ends using a pneumatic gripper and stretched at a displacement rate of 0.1 mm s^{-1}. The force–displacement curves of kirigami structures were measured experimentally and then the nominal stress–strain curves were derived from the dimensions of kirigami.

Next, the kirigami structure is numerically simulated by experimental and material analysis. In all simulations, the material behavior of the kirigami structure is obtained by using an elastic model (modulus of elasticity is 3000 MPa and Poisson's ratio is 0.4). The model is discretized using S4R cells and the width of the slit is set to 0.25 mm due to the incision width of the laser cutting machine in the experiment. The lower boundary of the model is fixed and vertical tensile displacement is applied to the upper boundary while there is no traction on the horizontal boundary. A static step is employed for the model. Due to local buckling instability during kirigami stretching, volume-proportional damping is added for convergence, and the dissipated energy fraction is set to 0.0005, with the maximum ratio of stabilization to strain energy set to 0.05.

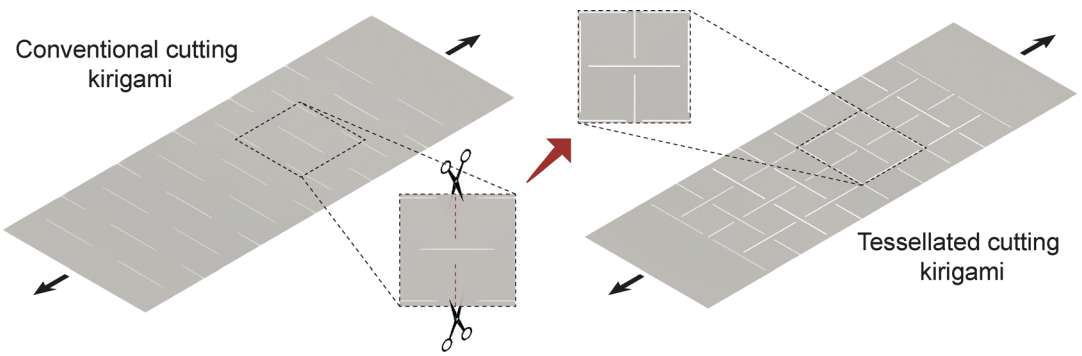

Fig. 2 Formation process of a tessellated cutting kirigami structure.

In the history output, the total dissipated energy and the total strain energy can be monitored to ensure that the ratio of the two is in a small range. This allows for more reliable results. Finally, to trigger structural instability, structural imperfections due to linear buckling are inserted at the initial stage of each simulation. A linear perturbation analysis is required to determine the critical buckling mode of the kirigami structure. Ten eigenvalues are solved for using the Lanczos eigenvalue solver. Based on the actual initial imperfections of kirigami test specimens, the scale factor is appropriately set to introduce imperfections in the form of critical modes to guide the post-buckling analysis.

The initial overall configuration and typical deformation configuration of the geometrically symmetric tessellated cutting kirigami structure are provided as shown in Fig. 3. The numerical simulation of the kirigami structure under tensile loading is in good agreement with the experimental configuration. Here the local buckling modes have been transformed from the symmetric and antisymmetric modes of the unidirectional cutting kirigami structure to the sheet and hinge buckling behaviors, evolving the interaction between the unidirectional cutting slits to the coupling between the sheet and the hinge. In Fig. 3(a), the buckling of the kirigami structure cut by the 0° slit under this action is mainly confined to the hinge section. In-plane hinge buckling and out-plane hinge buckling appears, while the sheet body is basically free of buckling deformation. The hinges are distributed alternately in two adjacent parallel planes. In Fig. 3(b), on the other hand, the buckling of the kirigami structure cut by the 45° slit under this action leads to deformation of both the hinges and the sheet, with the appearance of in-plane hinge buckling and out-of-plane sheet buckling. The different local buckling modes can be observed clearly from the locally enlarged front and lateral views of the kirigami structure. Therefore, the angle of the slit is one of the important coefficients used to describe the kinematics, and the observations on the tests are also validated constitutively by finite element simulations. It is worth noting that this stability is mainly determined by the geometric pattern and is not closely related to the material.

Fig. 4 shows the stress–strain response of these two typical geometrically symmetric kirigami structures for testing and simulation. In Fig. 4(a), the angle of the slit is parallel or perpendicular to the direction of the applied force such that the initial response of the specimen is linear. The overall structure is elastic at this stage. With increasing strain, all hinges buckled in-plane and the buckling of the hinges induced rotation and movement of the sheet. At this stage the sheet is involved in the rotation and movement causing the curve to reach a gentler stage. When the hinges complete out-of-plane buckling, the load-bearing force in the structure becomes dominated by the material, and the slope of the curve increases until the end of stretching. In Fig. 4(b), the angle of the slit is 45° with respect to the direction of the applied force, resulting in a smaller critical buckling force and a smaller range of sheet rotation. The hinge only provides a small amount of energy to move the sheet. This makes the elastic stage of the kirigami structure almost invisible, and it directly progresses to the gentle stage of the curve. The in-plane buckling

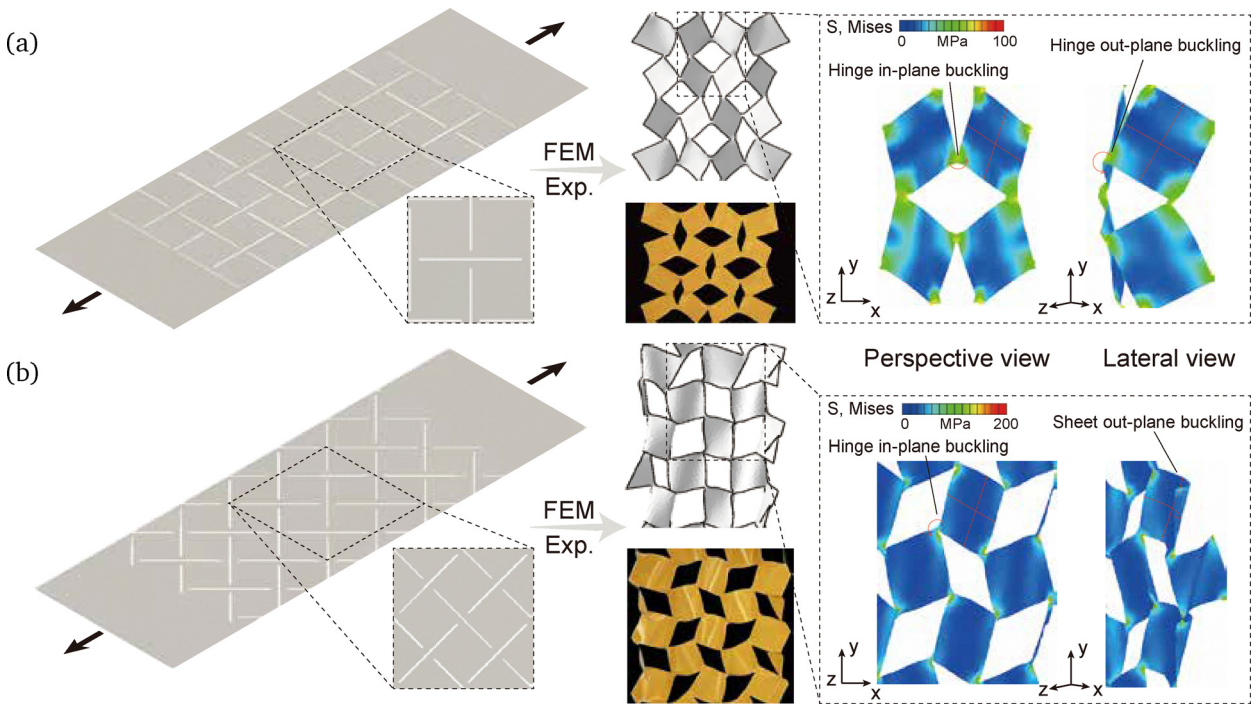

Fig. 3 Schematics of the initial overall and typical deformed configurations of geometrically symmetric tessellated cutting kirigami structures: (a) the kirigami structure cut by slit at 0° angle shows hinge in-plane buckling and hinge out-plane buckling. (b) The kirigami structure cut by slit at 45° angle shows hinge in-plane buckling and sheet out-plane buckling.

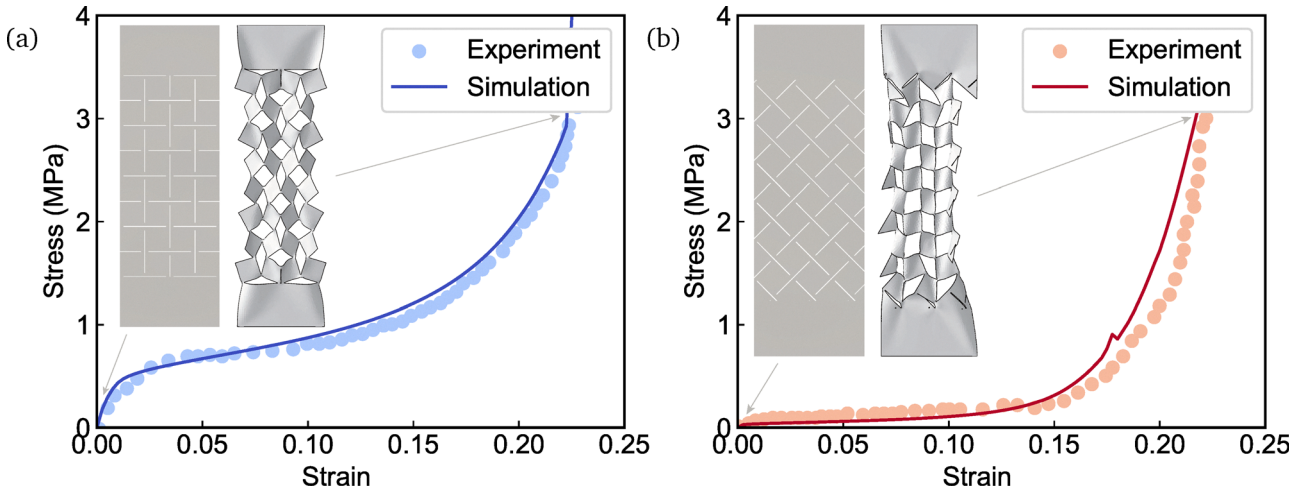

Fig. 4 Comparative validation between experiment and simulation of typical geometrically symmetric tessellated cutting kirigami structures: (a) kirigami structure with 0° angle slit. (b) Kirigami structure with 45° angle slit.

of the hinge has moved the sheet, and with a further increase in strain, the sheet begins to buckle out of plane, realizing a lengthening of the curve until the end of stretching.

3 Deep learning-assisted symmetry-breaking kirigami model

In order to facilitate the expression of the geometric features, the dimensions of the overall structure can be determined with the overall length of the kirigami L = 120 mm, the width W = 40 mm. Based on the above experimental groundwork, asymmetric kirigami structures with different single-cell patterns exhibit various mechanical behaviors and buckling modes under stretching. Several typical geometrically asymmetric kirigami structures are simulated as shown in Fig. 5. Its post-buckling nonlinear response changes with different single-cell patterns, in which this geometry-property relationship is yet to be explored and exploited. The stretchability of a kirigami structure is the maximum strain that the kirigami structure can achieve during the elastic stage.

3.1 Data generation for buckling kirigami

To capture the diversity and symmetry-breaking behaviour of the kirigami, as shown in Fig. 5(a), nine geometric parameters are successively introduced in the concept definition to describe the kirigami structure's single cell pattern: the spacing of the central vertical slit from the upper and lower horizontal slits δ_{up} and δ_{lo}, the spacing of the central vertical slit from the left and right horizontal slits δ_{le} and δ_{ri}, the deflection angle of the left and right horizontal slits θ_{le} and θ_{ri}, the deflection angle of the central vertical slit θ_{tr}, the overall deflection angle of the single cell θ_{ro} and the thickness of the kirigami structure t. The above nine geometric parameters can basically cover all the tessellated cutting kirigami structures in the form of a single cell, laying the foundation for the next refinement of the design space of kirigami structures. Fig. 5(b)–(e) shows four representative structural designs. Different patterns of kirigami structures can be achieved by adjusting the geometric parameters, both symmetric and asymmetric patterns are included, and the selection flexibility can be maximized. From these four representative structural designs, it can be seen that variations in the single-cell patterns can evoke changes in the mechanical properties of the kirigami structures such as stretchability, post-buckling behavior, strength and buckling mode, which indicates that the tensile mechanical behaviors and buckling modes of the kirigami structures are intensely affected by the variations in the single-cell geometries. This complex nonlinear relationship between geometry and property requires in-depth investigation.

The selection and transformation of these nine geometric parameters can theoretically produce geometric patterns for any kirigami structure. Because of this, the geometric pattern design space for kirigami structures is huge and vast. Theoretically, it is not possible to provide effective proposals for multi-parameter, high-complexity nonlinear responses, and the use of exhaustive experimentation or simulation to explore geometry–property interactions is equally unfeasible. A data-driven approach using deep learning is currently an effective manner. Instead of the traditional exhaustion method, this approach can be employed to predict the performance of kirigami structures that may have desirable mechanical properties, while minimizing the experimental and computational costs.

To achieve the removal of redundant workload and manufacturability, restrictions are imposed on these geometric parameters at the beginning of the model establishment. To facilitate the fabrication of the specimens, the ratio of the slit gap to the length of the single cell is set to 0.05 or more, which results in a clearer boundary between the hinge and the sheet, and the fabricated specimens are more satisfying to the process and test requirements. In this paper, the direction of the slits around the single cell is kept constant and its

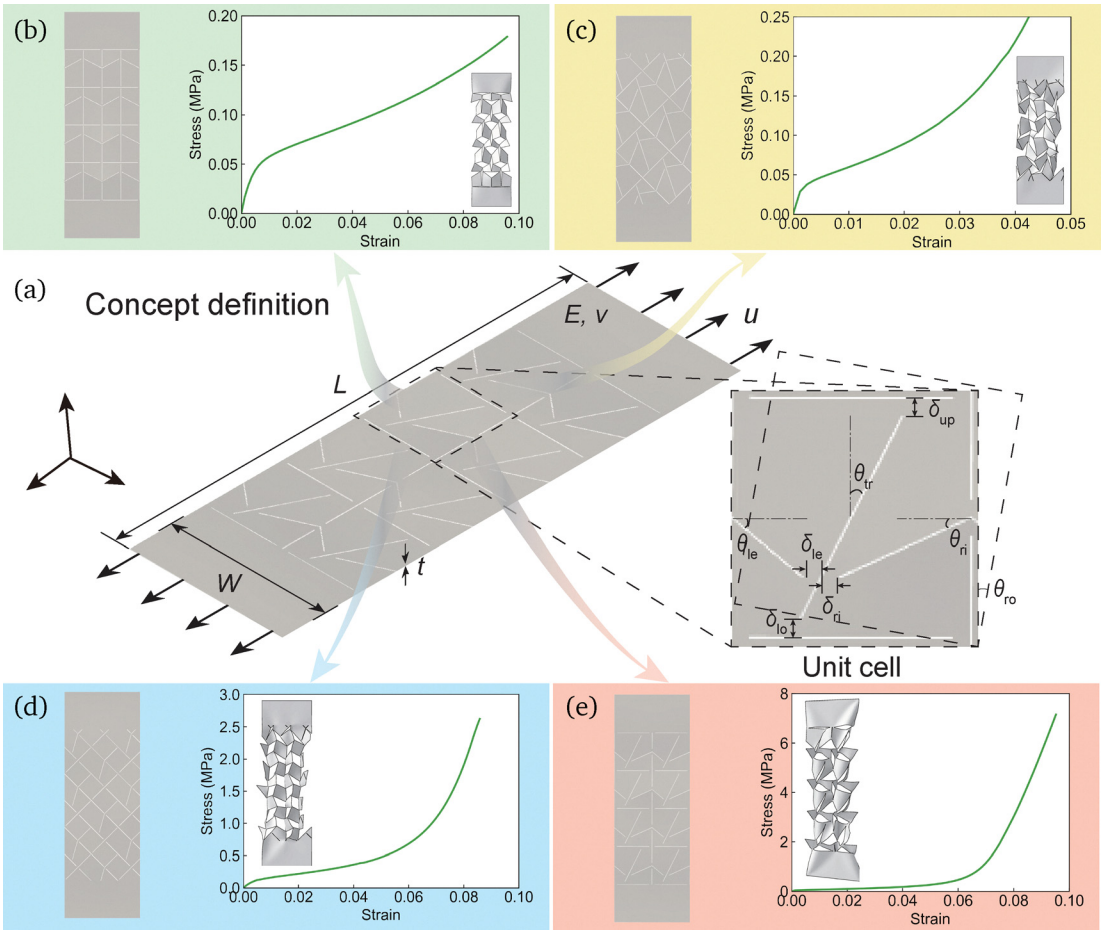

Fig. 5 Conceptual definition and representative structural designs of geometrically asymmetric tessellated cutting kirigami structures: (a) conceptual definition. (b)–(e) Four representative structural designs. It provides the vast design space for kirigami optimization and candidate structures to achieve optimized tensile performances in flexible and functional applications.

geometric parameters are limited as follows:

$$\begin{aligned} &\delta_{up} = \delta_{lo} = \delta_{le} = \delta_{ri} \in \{0.5, 1, 1.5\} \\ &\theta_{le} = \theta_{ri} \in \{-30^\circ, 0^\circ, 30^\circ\} \\ &\theta_{tr} \in \{0^\circ, 15^\circ, 30^\circ\} \\ &\theta_{ro} \in \{0^\circ, 45^\circ\} \\ &t \in \{0.05, 0.1\} \end{aligned} \tag{1}$$

Geometric asymmetry is explicitly defined by deviations in slit angles or spacings. When $\theta_{le} = \theta_{ri}$,$\delta_{le} = \delta_{ri}$, and $\theta_{tr} = 0^\circ$, it is a symmetric condition. Any violation of the above equality conditions is the asymmetric condition. For better selection and prediction, the purpose of traversing the entire design space can be achieved by using different permutations of the above nine geometric parameters. An initial database with 2916 different kirigami samples is constructed here. Each kirigami sample has a different geometric pattern and corresponding buckling response. Symmetry-breaking behavior can be realized by such an operation, which makes the mechanical response branching paths more abundant. The diversity of kirigami structural complexity is maintained and redundant designs can be avoided. The database is automatically generated based on a large number of simulations, and the process is code-controlled and requires no human intervention. The resulting database can be directly implemented in model construction without secondary operations and meets a broad range of design requirements.

At the initial database build-up stage, a large number of finite element simulations are conducted to characterize the tensile mechanical properties of the structures. In the simulations, the kirigami structures are gradually stretched, from a pre-buckling stage that embodies in-plane deformation to a post-buckling stage that reflects out-of-plane deformation when the tensile strain exceeds the critical buckling strain of the structure. Finally, the elongation reaches the tolerance range of the structural deformation until fracture of the material happens. Due to the computational complexity of the stretching process of the kirigami structure, the simulation is accordingly simplified in this paper. The number of grids, material types, *etc.* are adjusted to shorten the simulation time as much as possible without disturbing the results. This still allows an average time of 8 minutes per simulation on a CPU of Ryzen 9

12-core processor. From a mathematical point of view, the geometric pattern of the geometrically asymmetric kirigami structure can be infinitely varied by controlling the nine geometric parameters. To be representative of the geometric model and to diminish the numerical simulation effort, geometric restraints are imported in this paper. Although geometric restraints are used, a tremendous design space for representative kirigami structures can finally be produced under these geometric restraints, which also makes it possible to design the mechanical programmability of geometrically asymmetric kirigami.

3.2 Establishment of deep learning model

Fig. 6 presents a framework for the design of geometric asymmetric kirigami structures based on deep learning. During the model establishment process, the correspondence between the geometric pattern and the mechanical response is fitted in the format of data.

As shown in Fig. 6(a), each of the kirigami structures composed of single-cell pattern is numerically simulated to produce its corresponding buckling pattern and mechanical response. Buckling patterns are utilized for comparison and validation in framework design, and it is sufficient to ensure that there is a difference in buckling patterns between different kirigami structures. The geometric parameters and the mechanical responses, such as stress–strain curves, are pre-processed to generate arrays, which are then subjected to normalization, Principal Component Analysis (PCA), *etc.* The stress data with dimension 101 are extracted by PCA and then normalized. For the pre-processing of the stress data, the stress data with dimension 101 is compressed by principal component extraction and compressed into 10-dimensional vectors, which are then inputted into the output data. Cumulative explained variance (CEV) is defined as the ratio of the sum of the eigenvalues of the principal components to the sum of all the eigenvalues $\left(\sum_{i=1}^{10}\lambda_{ii}\Big/\sum_{i=1}^{101}\lambda_{ii}\right)$, and the computed value can be obtained is 99%. This value means that the 10-dimensional vector can represent the original 101-dimensional vector with 99% of its main components, and this data obtained through PCA dimensionality reduction operation can still represent the original data adequately for effective training after normalization.

As shown in Fig. 6(b), the main body of the deep learning model employs the deep neural network (DNN) architecture. The architecture is divided into input data, output data and unit layers. The original database was a huge array containing 2916 kirigami samples. Each kirigami sample has a set of geometric pattern parameters and a corresponding strain–stress buckling curve. Among them, the geometric pattern parameters and the strain array constitute the input data, and the stress array constitutes the output data, materialized as a stress array after PCA extraction and dimensionality reduction. 80% of the whole dataset is the training set, 10% is the validation set and 10% is the test set. The input data and output data are matched and verified against the corresponding buckling patterns. The unit layer of DNN is mainly composed of three sub-layers, namely: dense layer, batch normalization processing layer and activation layer. The dense layer is mainly used for extracting features, connecting features, assigning weights and fully connected transformations. The batch normalization processing layer helps to accelerate the

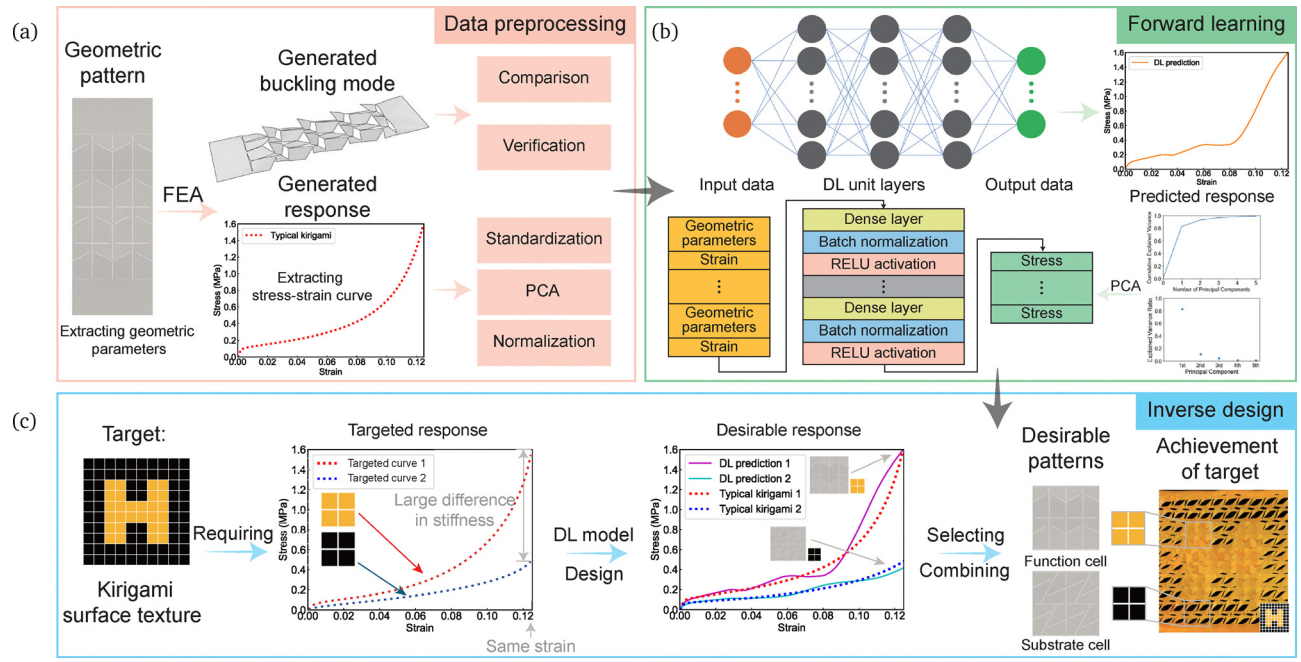

Fig. 6 A deep learning-based design framework for geometrically asymmetric kirigami structures: (a) data preprocessing. (b) Forward learning. (c) Inverse design.

training, reduce the sensitivity to the initial weights and has a regularization effect. The activation layer adopts an appropriate activation function, which can contribute to improving the nonlinearity of the model, and here the rectified linear unit (ReLU) activation function is adapted. The ReLU activation function is utilized with the MAE as the loss function. An Adam optimizer with a modulated learning rate is employed and the model is trained for 200 iteration steps. The forward learning is carried out by the deep learning model established above, and the model hyperparameters are iteratively tested and tuned until the result reaches a better performance.

After extensive forward learning, the model can be further applied to obtain inverse design of kirigami structures based on functional requirements. Fig. 6(c) gives an insight and example of an inverse design. The target function here is to realize a kirigami surface texture that enables display and encryption. Firstly, the functional requirements need to be quantified. Such a functional requirement can be realized by a variety of different kirigami cells combined on a metasurface. For simplicity, a combination of two different geometric patterns is used here. It should be noted that not every combination of arbitrary kirigami cells can achieve the desired functionality. This requires prediction and evaluation by a deep learning model. These two geometrically patterned kirigami structures need to have similar tensile strains and large differences in stress–strain responses. Only a combination of kirigami structures with such target responses can satisfy the requirement. Next, the target response with a maximum strain of 0.125 and a ratio of maximum stress between kirigami cells greater than 3 is used as model input. Through continuous iteration and evaluation of the model, the model can output the geometric parameters of the kirigami cells that meet the target response. Finally, validation and cells combination are carried out through experiments, which leads to the inverse design of kirigami surface texture.

3.3 Model hyperparameter screening and framework optimization

The mean absolute error (MAE) can be used as a loss function and is a measure to express the extent to which the predicted values of a model do not agree with the real values. MAE can be calculated by the following formula:[42]

$$\mathrm{MAE} = \frac{1}{n}\sum_{i=1}^{n}|e_i| \tag{2}$$

where n is the number of samples and model errors of samples are calculated as e_i, $i = 1, 2, \ldots, n$.

In the hidden layer, the activation function is chosen, containing ReLU activation function[43] in the following format:

$$\text{ReLU function} \quad f(x) = \max(0, x) \tag{3}$$

A hyperparameter analysis is conducted to finalize the appropriate number and size of hidden layers for optimization of the model's performance. During the data preprocessing stage, the input data (*i.e.*, geometric description parameters and deformation paths of the kirigami structure), as well as the output data (*i.e.*, stresses) in the database, are necessary to be normalized to the range [0,1]. This normalization process promotes model training and enhances accuracy. Based on the mentioned process, a deep learning model is built and trained to produce a non-linear correlation between geometric parameters and mechanical performances in the database. The datasets for training and validation in the deep learning model, *i.e.*, the training and validation sets, comprise 80% and 10% of the database, respectively, and the residual 10% is assigned to the test set. Finite element modeling of the kirigami structures is carried out and then the deep learning model is executed to predict their tensile performances. The loss function used during training is intended to quantify the difference between the deep learning model predictions and the finite element simulation results. Through iterations, the loss calculating function is gradually updated and approaches the ultimate value, which demonstrates the effectiveness of the deep learning model in approximation to the numerical simulation results. The training model is further validated effectively. As the iteration step continues, the predicted mechanical response can be well-matched with the output data of the test set. As the number of neurons or layers in the model is adequately increased, the deep learning model becomes more complicated but the value of calculated loss within the training set is reduced. This appropriate level of model complexity improves the accuracy of the model without overfitting or underfitting.

With consideration of aspects such as dropout layers, normalization process and optimization algorithms, the hyperparameters and structural configurations of the proposed deep learning model are optimized. The performance of the DNN depends strongly on the choice of its hyperparameters. Hyperparameters are parameters set before the learning process, which are distinguished from the parameters acquired through learning process during the training of the model. Hyperparameters are mainly related to the learning rate, the number of iterations, the number and size of hidden layers, the batch size, the choice of activation function, *etc.* These hyperparameters can significantly influence the learning capability and generalization ability of their models. Fig. 7 shows the effect of the two main hyperparameters, *i.e.*, the number of hidden layers and the number of neurons, on the performance of model. Fig. 7(a) provides results for various numbers of stacked layers, evaluated using MAE. Local zoom-in results from the end of the iteration step in the figure reveal that the performance of the test set for a single layer fluctuates relative to the training set. Moreover, the 5-layer model is not as efficient as the 3-layer model in terms of prediction, but the former needs more training time and computational effort. Therefore, a DNN architecture with 3 hidden layers is employed in this paper. Meanwhile, Fig. 7(b) shows that the model with 500 neurons per layer exhibits better performance in comparison with the models with 100 and 1000 neurons. Hence, as shown in Table 1, based on the analysis of hyperparameters and configurations, the optimal settings for the DNN

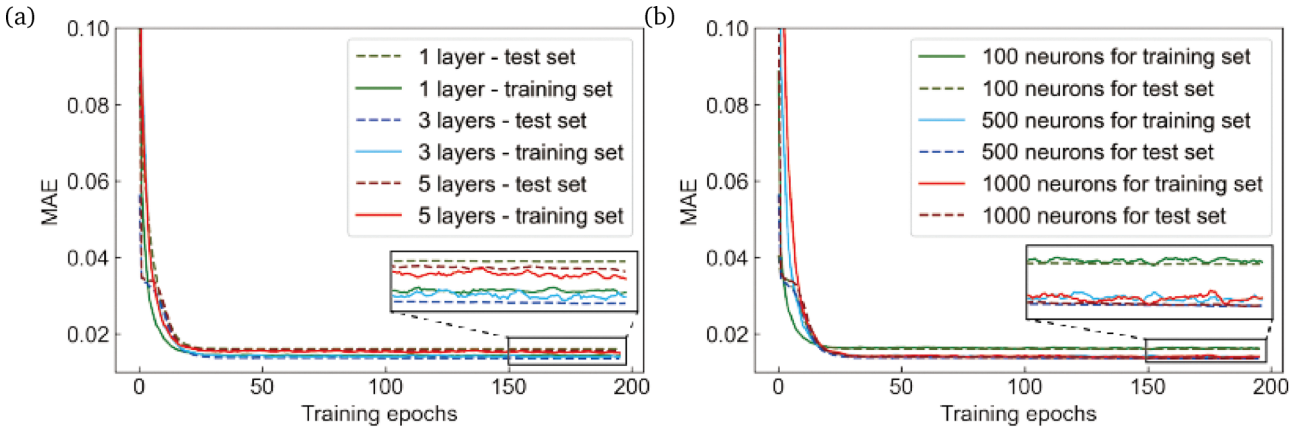

Fig. 7 The results of hyperparameter analysis and prediction performance of the selected DNN model: (a) the number of layers of the DNN model. (b) Number of neurons in DNN model.

Table 1 Performance comparison of DNN models

Model	Epochs	Optimizer	Batch size	Layers	Neurons	MAE-training set	MAE-test set
DNN-1	200	Adam	64	1	500	0.0144	0.0160
DNN-2	200	Adam	64	3	500	0.0139	0.0136
DNN-3	200	Adam	64	5	500	0.0154	0.0154
DNN-4	200	Adam	64	3	100	0.0160	0.0160
DNN-5	200	Adam	64	3	1000	0.0140	0.0136

architecture are 3 hidden layers and 500 neurons per layer by which the best learning capability and generalization results can be achieved.

3.4 Model accuracy and error analysis

After simulation and experimental validation of unique types of geometrically asymmetric kirigami structures, a deep learning model is established and well-regulated hyperparameters are set up so that the model has good learning and generalization capabilities. In this subsection, the performance of the deep learning model is analyzed.

In this paper, the DNN architecture involves several multi-level hidden layers. This hidden layer design improves the precision comparing to other model architectures by enabling the architecture to use solid data after a series of operations to fit the time-dependent nonlinear mechanical response. Significantly, deep learning models can offer faster predictions than numerical simulations. For instance, the generated deep learning model takes only 20 ms to predict the mechanical response of the kirigami structure on the basis hardware of an NVIDIA GeForce RTX 2070, whereas a numerical simulation running on a CPU of a Ryzen 9 12-core processor requires an additional 8 minutes on average. In general, the actual computation time can be reduced by hardware upgrades, but it is evident that the magnitude of the reduction is still in the same order. DNN architecture is adopted to predict and gain tensile mechanical performances of kirigami structures with various geometric patterns instead of relying only on numerical simulations that are complicated to debug and difficult to converge. It is also a novel attempt to explore and demonstrate.

After optimization of the hyperparameters and configurations of the proposed developed deep learning model, the model is further assessed for its performance. Fig. 8 presents

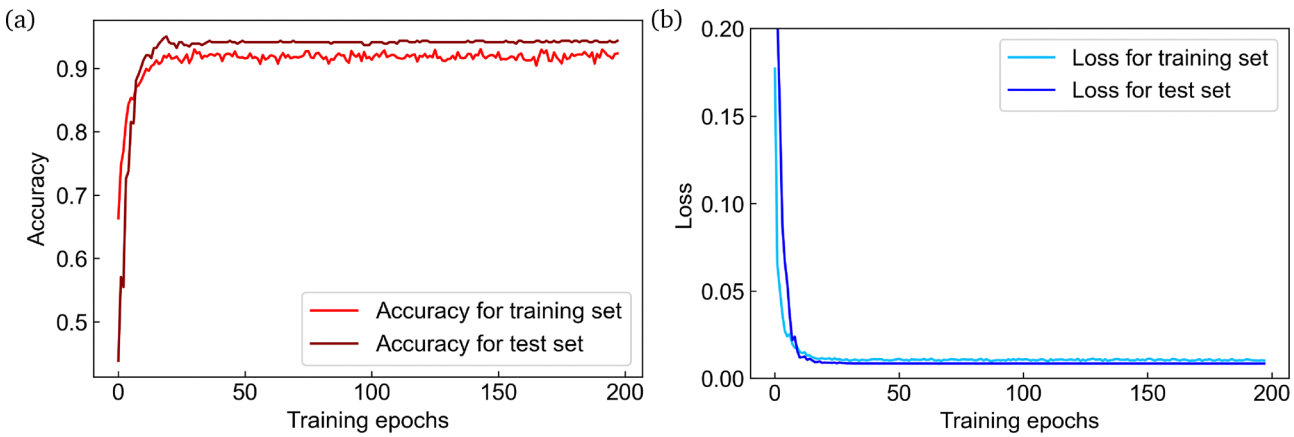

Fig. 8 The performance prediction of results of deep learning models for training and test sets: (a) accuracy. (b) Loss.

the performance prediction of the deep learning model for the training results of the training set and the test set. Fig. 8(a) and (b) illustrates two critical prediction evaluation metrics: accuracy and loss, for both the training and test sets.

After 200 iteration steps of training, the prediction accuracy and loss of both the training and test sets reach a more steady level. In this case, the accuracy of the training set and test set is 92.29% and 94.29%, respectively, and the loss values of both the training set and test set are quite low, 0.01012 and 0.008424, respectively. Here the test set is more accurate and has better generalization ability. The values of accuracy for both training and test set are above 90%, there is no overfitting and underfitting issues, and the results of the trained model are relatively favorable.

4 Results and discussion

In this section, the mechanical programmability of the kirigami structure is demonstrated by using the fine-tuned model. Then, the results obtained from the deep learning model are used to design functional kirigami and explore the potential applications in terms of their functionality.

4.1 Design and analysis of mechanical programmability

For kirigami structures with asymmetric geometric patterns, a large number of studies are carried out in this paper to investigate their mechanical behaviors under uniaxial stretching by altering the geometric parameters within a reasonable range. The design space generated by different dimensions of geometric parameters can create opportunities for the design of mechanical programmability of kirigami structures. In the post-buckling mechanical response of different kirigami structures, the stiffness variation tends to increase or decrease with the growth of tensile strain. The abundant geometric patterns correspond to abundant post-buckling mechanical responses, forming a vast design space that is the foundation of programmable design. Next, based on this programmability, the matching relationship between geometry and mechanical response is integrated with functional requirements.

This paper presents only one concept to demonstrate the actual functionality of the programmable design. The model is trained using a database of 2916 kirigami structures that are representative and numerous enough to occupy a design space. After adjusting the iterative model and training, the optimized model is applied to search for specific structures. Fig. 9(a) illustrates the probability distribution of the tensile strains of

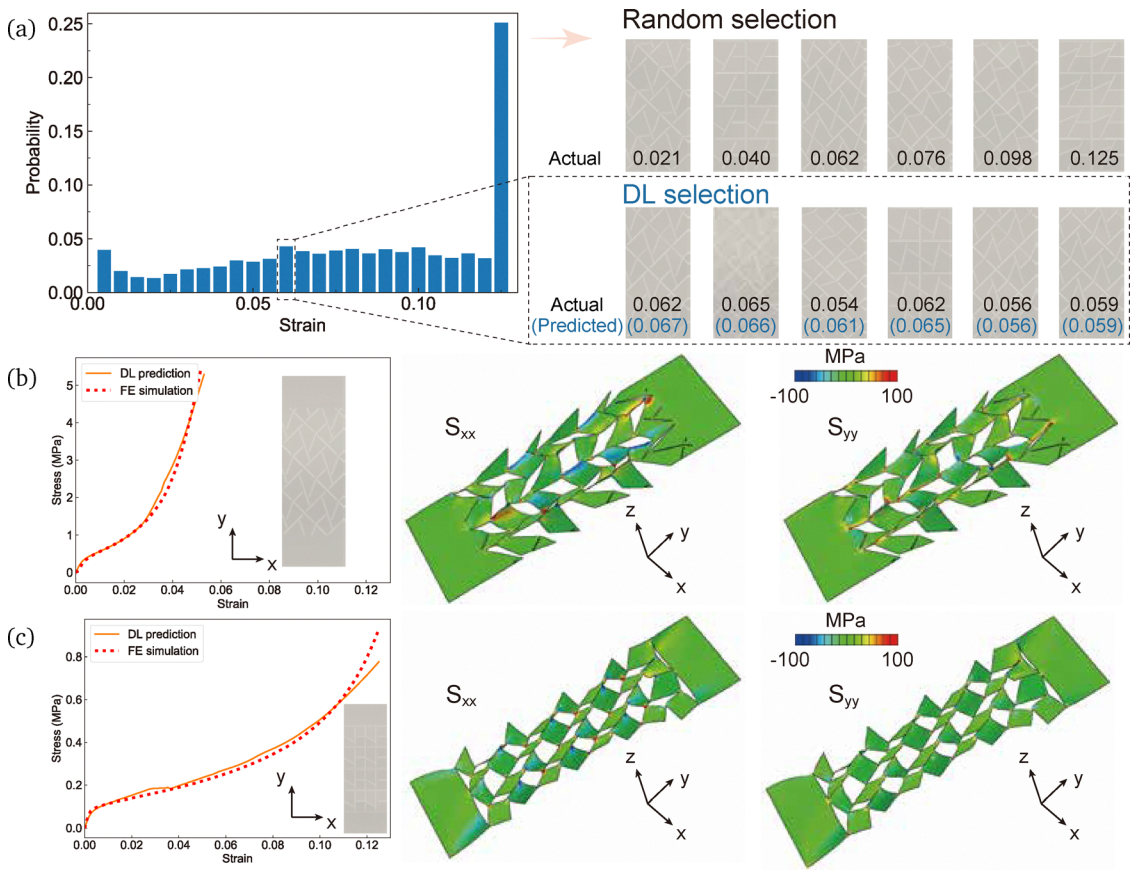

Fig. 9 Tensile strain probability distribution plots and typical results: (a) tensile strain probability distribution plots for 2916 kirigami structures and comparison between random selection and DL selection. (b) and (c) Comparison between deep learning models and finite element simulations for two typical kirigami structures.

these 2916 kirigami structures, which quantifies the chances of obtaining a kirigami structure of the desired tensile strain in a randomly selected case from a probabilistic point of view. From the distribution plots, it can be seen that most of the geometric patterns allow the stretchability of the kirigami structures to be enhanced, but the geometric patterns of some special kirigami structures (kirigami structures with tensile strains less than 0.02) do not improve the stretchability of the structures. And the structures that still mainly show the brittleness of the material in tension indicate that such slit types do not have any effect on the structural stretchability. This may be due to the lack of interaction between the slits resulting from the geometric pattern itself, or it may be that the angle between the slits and the tensile direction results in stress concentrations that lead to no growth in the stretchability of the structure. Randomly selecting kirigami structures with different geometric patterns can yield random tensile strain responses, which is a time-consuming and laborious exhaustive attempt. For example, if a kirigami structure with a tensile strain of 0.06 is required, the deep learning model can be guided to identify kirigami structures with specific geometric patterns that are close to the results. Moreover, its predicted results are more closely fitted to the reality (black numbers represent actual tensile strains and black numbers represent predicted tensile strains). With this model, other different tensile strains are available. Further, the kirigami structures of different geometric patterns under quantifiable mechanical properties can be obtained inversely by this model.

Next, Fig. 9(b) and (c) shows the comparison of two typical kirigami structures between the deep learning model and the numerical simulation. Kirigami structures of the same size with different geometric patterns produce different strain–stress responses after stretching. Compressive stresses in addition to localized tensile stresses are observed near the edges of the slit in both x and y directions. Since the structure has no out-of-plane constraints, the existence of compressive stresses induces local out-of-plane deformation in the nearby region as a measure to release the stored energy of the system and reduce the tensile stresses in the proximity of the slits. This out-of-plane buckling deformation varies with the overall geometric pattern design of the structural system. The appearance of out-of-plane deformation increases the stretchability of the structure and enters a post-buckling stage until a threshold of structural deformation is reached. The kirigami structure without out-of-plane deformation is not able to release the energy due to stretching well even though there are also slits existing on the surface, *i.e.*, the material is required to afford this portion of the energy, which shows brittleness on a macroscopic level.

4.2 Verification and regulation of tensile mechanical behavior

After investigating geometric nonlinear kirigami structures, this subsection provides a strategy for functional design of kirigami structures by using deep learning models. Firstly, to achieve the demand of kirigami textured patterns, decomposition and single-cell classifications of kirigami structures on functional surfaces are required. Taking two kirigami cells as an example. As shown in Fig. 10(a), if "HIT" is displayed on the textured pattern, the two types of cells can be the functional cell (yellow) that displays the letters and the backing cell (black) that displays the background, and the kirigami textured pattern is composed of these two types of cells. Finally, the mechanical response of the kirigami structure composed of the two types of cells is explored and selected. For the formation of the desired texture patterns, the selection principles are provided in this paper: (1) the tensile strains between the single cells need to be consistent or similar. (2) The ratio of the overall tensile stiffness between the single cells is over 3. As shown in Fig. 10(a) and (b), the deep learning model can select two kinds of single cells and predict the stress–strain curves. According to the selection principle, two target curves can be given. Although the deep

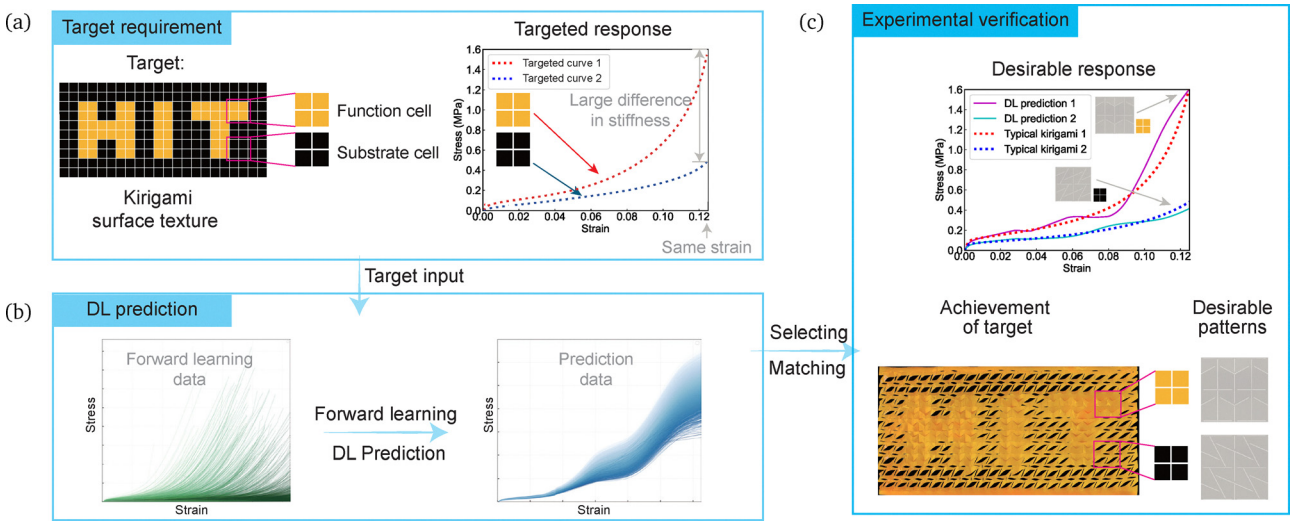

Fig. 10 An inverse design strategy using deep learning framework for functional requirements: (a) functional requirements. (b) Forward learning and prediction. (c) Matching and experimental verification.

learning model can predict the mechanical response of the arbitrary kirigami, identifying the target curves and matching the appropriate mechanical response requires an inverse design strategy. For this purpose, the trained model can effectively solve this inverse design problem. To better explore the design space, we predicted 3000 completely arbitrary related curves. To identify and match the target curve, we select the predicted curve with the smallest error relative to the target curve as the optimal curve. Next, as shown in Fig. 10(c), we inversely derive the geometric pattern of the kirigami structure corresponding to the optimal curve. The functional experiment is conducted for verification.

As can be seen in Fig. 11(a) and (b), the predicted curves gradually approach the target curve. The optimized curves are finally obtained. Numerical simulations are conducted to verify the nonlinear mechanical behavior of the kirigami structure resulted from these two single cell arrays. The predicted trend and the final results can better meet the actual requirements. The buckling modes of the kirigami structures can be seen shown in the inset. After identifying the mechanical responses, the geometric patterns of the two ideal kirigami structures with their single cells can be inversely designed. By combining the two patterns designed above, the kirigami surface of Fig. 11(c) can be created, which is generated by the regular arrangement of the function cells and the substrate cells in accordance with the thumbnail in the upper left corner of the figure. The assembled kirigami structure which is created in this manner has the function of off-angle display and encryption in a normal camera perspective. When the kirigami structure is not stretched, the surface of the structure appears to be uniform and without any information display. After stretching, the "HIT" information can be observed from the view a, which is positively angled to the x–y plane, with the 45° angle being the best viewing angle. Correspondingly, when viewed from view b, a negative angle with the x–y plane, no valid information can be observed, especially at the −45° angle, which is the best observing angle, and it can be effective to display or encrypt the off-angle view.

In addition to exhibiting selective visibility from a normal camera perspective, the thermal camouflage functionality can also be achieved. The thermal information observation test employs infrared cameras to capture uniform physical fields from various observation positions. By altering the angle and location of observation, thermal information can be readily

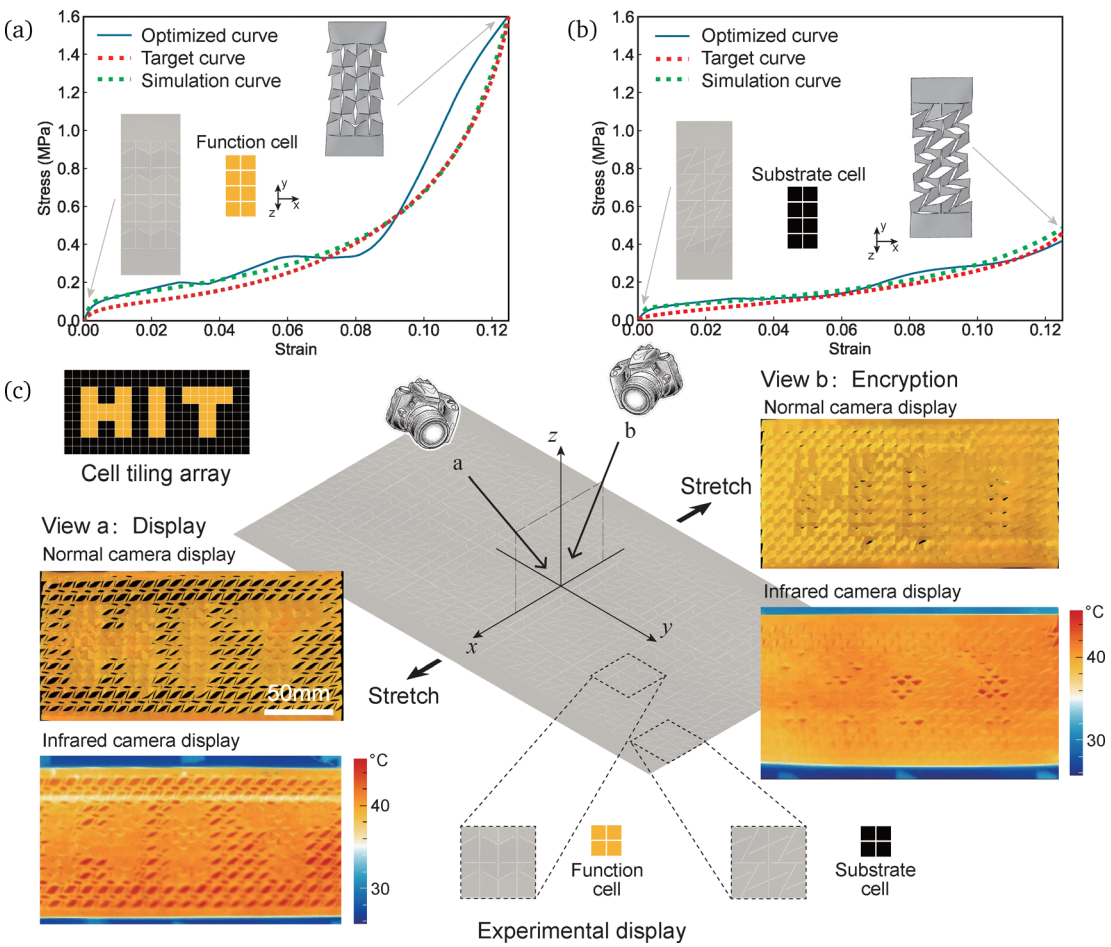

Fig. 11 Design and functional implementation of textured patterns for kirigami structures: (a) and (b) selection of two kirigami structural cells and their nonlinear responses. (c) Functionality of textured pattern tessellation achievable by combination of two kirigami structural cells.

discerned at the −45° angle, whereas it remains indistinguishable from other positions. The emergence of this functionality is mainly the result of the inconsistency of the buckling patterns of the two single cells and the utilization of the different buckling patterns. Only the kirigami structure and its functional display of the combination of two single cells are shown here. More complex display possibilities can also be explored by the same procedure. For instance, a kirigami structure combined with three or more cells can be available to display different information at different stages of stretching and viewing angles. The kirigami structure can be made of elastic materials, and the overall system can be stretched repeatedly over a number of cycles without plastic deformation. The accuracy of the information displayed after repeated stretching is still high enough to be recognized and read by humans and machines for further information transfer.

5. Conclusions

In this paper, a deep learning model-based geometric design method for the kirigami structure is proposed. The strategy provides programmable design solutions for generating the corresponding mechanical responses of the desired kirigami structure. A deep learning model with a vast design space, which contains the geometric patterns and constitutive relations of thousands of typical kirigami structures, is developed using kirigami structure tests for validation and simulation results as the basic data. This data-driven strategy accurately predicts complex nonlinear constitutive relations by effectively managing large data sets. By extracting the stress–strain curves of the kirigami structure, the DNN model takes the form of a direct correlation matrix to efficiently handle nonlinear data and establish the link between geometric and constitutive relations. Optimal model performance is achieved by configuring the DNN model with 3 hidden layers, 500 neurons and dropout layers. After 200 iterations, the prediction loss, metric and error of the training and test sets have been reduced to the desired level and the model has good prediction accuracy.

The mechanically programmable design solution and the strain probability distribution diagram for this kirigami structure are given. The geometric patterns of the kirigami structures are quantified according to the required strain demand, and the range of geometric pattern can be targeted and limited. At the same time, the exclusion of undesired geometric patterns improves the demand adaptability of the required mechanical response, increases the probability of realization and reduces the cost associated with exhaustive experimental simulations. The design method allows the design of various kirigami structures to meet different functional requirements. To prove the applicability of the method, it is applied to kirigami textured patterns. The functional design of the kirigami surfaces is achieved by this design method, and the combination of two selected kirigami cells can be displayed and encrypted in the perspectives of normal and infrared cameras. Such customizable kirigami structures with stretched display and encryption can be used in the field of flexible multifunctional integrated device manufacturing and in the field of diagnostics and novel information encoding and delivery.

Conflicts of interest

There are no conflicts to declare.

Data availability

The experimental data and FEA simulations containing details of the finite element model setup, specimen for uniaxial tests are available in the article. The script files for the DL models are available from the authors upon reasonable request.

Acknowledgements

The authors acknowledge financial support from the National Natural Science Foundation of China (Grant No. 12172102, 12202105, 12202222), Shenzhen Basic Research Program under Grant No. JCYJ20240813094159001 and Postdoctoral Fellowship Program of CPSF under Grant No. GZC20251284.

References

1 X. Yang, C. Forró, T. L. Li, Y. Miura, T. J. Zaluska, C.-T. Tsai, S. Kanton, J. P. McQueen, X. Chen and V. Mollo, *et al.*, *Nat. Biotechnol.*, 2024, 1–8.
2 L. Jin and S. Yang, *Adv. Mater.*, 2024, **36**, 2308560.
3 Y. Zhang, Y. Wang, Q. Tao, Y. Liu and C. Wang, *Int. J. Mech. Sci.*, 2024, **280**, 109331.
4 R. He, Y. Chen, J. Shi, Y. Bai and J. Feng, *Thin Wall Struct.*, 2025, **207**, 112706.
5 W. Wang, C. Li, H. Rodrigue, F. Yuan, M.-W. Han, M. Cho and S.-H. Ahn, *Adv. Funct. Mater.*, 2017, **27**, 1604214.
6 Y. Tang, G. Lin, S. Yang, Y. K. Yi, R. D. Kamien and J. Yin, *Adv. Mater.*, 2017, **29**, 1604262.
7 N.-S. Jang, K.-H. Kim, S.-H. Ha, S.-H. Jung, H. M. Lee and J.-M. Kim, *ACS Appl. Mater. Interfaces*, 2017, **9**, 19612–19621.
8 Y.-S. Guan, H. Li, F. Ren and S. Ren, *ACS Nano*, 2018, **12**, 7967–7973.
9 Q. Li, W. Liu, C. Yang, P. Rao, P. Lv, H. Duan and W. Hong, *J. Mech. Phys. Solids*, 2022, **169**, 105053.
10 X. Hong, B. Xu, G. Li, F. Nan, X. Wang, Q. Liang, W. Dong, W. Dong, H. Sun and Y. Zhang, *et al.*, *Sci. Adv.*, 2024, **10**, eadn7582.
11 L. Hong, H. Zhang, T. Kraus and P. Jiao, *Adv. Sci.*, 2024, **11**, 2303674.
12 S. Hou, C. Chen, L. Bai, J. Yu, Y. Cheng and W. Huang, *Small*, 2024, **20**, 2306749.
13 T. C. Shyu, P. F. Damasceno, P. M. Dodd, A. Lamoureux, L. Xu, M. Shlian, M. Shtein, S. C. Glotzer and N. A. Kotov, *Nat. Mater.*, 2015, **14**, 785–789.
14 J.-H. Low, P.-S. Chee, E.-H. Lim and V. Ganesan, *Smart Mater. Struct.*, 2024, **33**, 025029.

15 T.-H. Chen, Y. Hong, C.-T. Fu, A. Nandi, W. Xie, J. Yin and P.-C. Hsu, *PNAS nexus*, 2023, **2**, pgad165.
16 Y. Wang and C. Wang, *Int. J. Solids Struct.*, 2021, **213**, 93–102.
17 H. Taniyama and E. Iwase, *Micromachines*, 2019, **10**, 395.
18 A. Rafsanjani and K. Bertoldi, *Phys. Rev. Lett.*, 2017, **118**, 084301.
19 J. Gu, J. Ahn, J. Jung, S. Cho, J. Choi, Y. Jeong, J. Park, S. Hwang, I. Cho and J. Ko, *et al.*, *Nano Energy*, 2021, **89**, 106447.
20 A. Rafsanjani, Y. Zhang, B. Liu, S. M. Rubinstein and K. Bertoldi, *Sci. Rob.*, 2018, **3**, eaar7555.
21 S. Babaee, Y. Shi, S. Abbasalizadeh, S. Tamang, K. Hess, J. E. Collins, K. Ishida, A. Lopes, M. Williams and M. Albaghdadi, *et al.*, *Nat. Mater.*, 2021, **20**, 1085–1092.
22 S. Babaee, S. Pajovic, A. Rafsanjani, Y. Shi, K. Bertoldi and G. Traverso, *Nat. Biomed. Eng.*, 2020, **4**, 778–786.
23 Z. Rao, Y. Lu, Z. Li, K. Sim, Z. Ma, J. Xiao and C. Yu, *Nat. Electron.*, 2021, **4**, 513–521.
24 Y. Yang, M. A. Dias and D. P. Holmes, *Phys. Rev. Mater.*, 2018, **2**, 110601.
25 K. Guo, Z. Yang, C.-H. Yu and M. J. Buehler, *Mater. Horiz.*, 2021, **8**, 1153–1172.
26 B. Sanchez-Lengeling and A. Aspuru-Guzik, *Science*, 2018, **361**, 360–365.
27 P. Cai, C. Wang, H. Gao and X. Chen, *Adv. Mater.*, 2021, 2007977.
28 J.-W. Su, D. Li, Y. Xie, T. Zhou, W. Gao, H. Deng, M. Xin and J. Lin, *Smart Mater. Struct.*, 2020, **30**, 015028.
29 G. X. Gu, C.-T. Chen, D. J. Richmond and M. J. Buehler, *Mater. Horiz.*, 2018, **5**, 939–945.
30 X. Li, S. Ning, Z. Liu, Z. Yan, C. Luo and Z. Zhuang, *Comput. Methods Appl. Mech. Eng.*, 2020, **361**, 112737.
31 C.-T. Chen and G. X. Gu, *Adv. Sci.*, 2020, **7**, 1902607.
32 T. Zhao, Y. Li, L. Zuo and K. Zhang, *Extreme Mech. Lett.*, 2021, **45**, 101297.
33 Y. Zhang, Q. Tao, Y. Liu and C. Wang, *Compos. Sci. Technol.*, 2022, **230**, 109735.
34 S. Yang, W. Yao and L.-L. Ke, *et al.*, *Thin Wall Struct.*, 2025, **207**, 112718.
35 Z. Yang, C.-H. Yu, K. Guo and M. J. Buehler, *J. Mech. Phys. Solids*, 2021, 104506.
36 P. Rajak, B. Wang, K.-I. Nomura, Y. Luo, A. Nakano, R. Kalia and P. Vashishta, *npj Comput. Mater.*, 2021, **7**, 102.
37 A. Challapalli, J. Konlan and G. Li, *Int. J. Mech. Sci.*, 2023, **244**, 108029.
38 M. Zhao, X. Li, X. Yan, N. Zhou, B. Pang, B. Peng and Z. Zeng, *Thin Wall Struct.*, 2025, **208**, 112845.
39 N. A. Alderete, N. Pathak and H. D. Espinosa, *npj Comput. Mater.*, 2022, **8**, 191.
40 H. Guo and J. Zhang, *Adv. Mater.*, 2025, **37**, 2412064.
41 P. Z. Hanakata, E. D. Cubuk, D. K. Campbell and H. S. Park, *Phys. Rev. Lett.*, 2018, **121**, 255304.
42 T. Chai and R. R. Draxler, *Geosci. Model Dev.*, 2014, **7**, 1247–1250.
43 A. F. Agarap, *arXiv*, 2018, preprint, arXiv:1803.08375, DOI: 10.48550/arXiv.1803.08375.

